Bioactive Materials 53 (2025) 641–655

Contents lists available at ScienceDirect

Bioactive Materials

journal homepage: www.keaipublishing.com/en/journals/bioactive-materials

Metabolic modulation-driven self-reinforcing pyroptosis-STING nanoadjuvant for potentiated metalloimmunotherapy

Linzhu Zhang [a,b,1], Di Wang [b,c,1], Yiming Liu [a,1], Nailin Yang [b,*], Shumin Sun [b], Chunjie Wang [b], Duo Wang [a], Jihu Nie [b], Juan Qin [a], Lei Zhang [a,**], Liang Cheng [b,***], Haidong Zhu [a,****]

[a] Center of Interventional Radiology & Vascular Surgery, Department of Radiology, Nurturing Center of Jiangsu Province for State Laboratory of AI Imaging & Interventional Radiology (Southeast University), Basic Medicine Research and Innovation Center of Ministry of Education, Zhongda Hospital, Medical School, Southeast University, 87 Dingjiaqiao Road, Nanjing, 210009, China

[b] Institute of Functional Nano & Soft Materials (FUNSOM), Jiangsu Key Laboratory for Carbon-Based Functional Materials & Devices, Soochow University, Suzhou, 215123, China

[c] Department of Interventional Radiology, The Second Affiliated Hospital of Soochow University, Suzhou, 215004, China

ARTICLE INFO

Keywords:
Pyroptosis
cGAS-STING pathway
Glucose metabolism
CoF_2 nanoenzymes
Transarterial embolization

ABSTRACT

Pyroptosis is a critical process that triggers inflammatory responses and mitochondrial DNA (mtDNA) release, thereby activating the cGAS-STING pathway. However, tumor metabolism, particularly glycolysis, often suppresses immune activation. To address this, we developed $GOCoF_2$, a self-amplifying pyroptosis-STING nanoadjuvant that integrates glucose oxidase (GOx) with cobalt fluoride (CoF_2) nanoenzymes. This nanoadjuvant excelled in converting intratumoral H_2O_2 into reactive oxygen species (ROS), inducing cell pyroptosis. Its self-sustaining mechanism involved glucose depletion and continuous H_2O_2 generation, ensuring persistent catalytic activity. This metabolic manipulation and induction of oxidative stress significantly enhance pyroptosis in tumor cells. The released mtDNA subsequently activated the cGAS-STING pathway, with Co^{2+} further amplifying this effect. Notably, glucose-dependent TREX2 inhibition intensified cGAS-STING activation through metabolic regulation, leading to a strong immune response and tumor growth suppression. When combined with immune checkpoint blockade therapy, $GOCoF_2$ significantly inhibited primary and distant tumor progression via systemic immune activation. Additionally, we formulated $GOCoF_2$-lipiodol for transarterial embolization, which demonstrated superior efficacy in a rat model of orthotopic hepatocellular carcinoma. This study not only sheds light on the intricate relationship between tumor metabolism and immune regulation but also introduces a novel therapeutic approach for hepatocellular carcinoma.

1. Introduction

Hepatocellular carcinoma (HCC) is a prominent contributor to global cancer-related deaths, maintaining a persistent substantial disease burden [1]. The insidious nature of HCC onset, coupled with its aggressive behavior, high metastatic potential, and frequent recurrence, leads to a troubling scenario in which nearly 70 % of patients are diagnosed only in the mid-to-late stages [2]. This delayed detection frequently results in missed opportunities for potentially curative interventions like surgical resection and radiotherapy. Emerging trends in HCC management have led to a marked increase in the clinical adoption of minimally invasive interventional approaches, notably transarterial embolization (TAE) and its chemotherapeutic counterpart, transarterial chemoembolization (TACE) [3–5]. While these localized therapies

Peer review under the responsibility of editorial board of Bioactive Materials.

* Corresponding author.
** Corresponding author.
*** Corresponding author.
**** Corresponding author.
E-mail addresses: nlyang@suda.edu.cn (N. Yang), zhang_lei@seu.edu.cn (L. Zhang), lcheng2@suda.edu.cn (L. Cheng), zhuhaidong@seu.edu.cn (H. Zhu).
[1] These authors contributed equally to this work.

https://doi.org/10.1016/j.bioactmat.2025.07.040
Received 12 May 2025; Received in revised form 11 July 2025; Accepted 22 July 2025

effectively curtail primary tumor proliferation, their efficacy is limited against disseminated and recurrent lesions [6]. The metabolic landscape of neoplastic tissues presents a stark contrast to the normal cellular environment, characterized by altered metabolic pathways and vascular irregularities [7,8]. A predominantly observed phenomenon in various malignancies is the augmentation of aerobic glycolysis, which is commonly termed the Warburg effect [9–13]. This metabolic shift is intricately linked with cancer stem cell maintenance, tumor progression, metastatic spread, and the development of therapeutic resistance [14,15]. The metabolic adaptation toward aerobic glycolysis in neoplastic cells has far-reaching consequences, particularly in the context of immune system evasion [16]. Within the tumor microenvironment (TME), a competitive interplay emerge between tumor cells and immune cells for essential nutrients [17]. The aberrant glycolytic pathway in cancer cells directly influences the expression of various immunoregulatory molecules [18]. Furthermore, the metabolic byproducts of aerobic glycolysis, such as lactate, exert suppressive effects on T-cell proliferation by interfering with the glycolytic machinery [19]. Concurrently, lactate generated via the Warburg effect serves as a critical endogenous modulator of tumorigenesis, promoting the expansion of the cancer stem cell population by suppressing their differentiation and inducing cancer differentiated cells into a proliferative cancer stem cell phenotype [20]. Given these insights, the strategic modulation of tumor metabolism, particularly through targeted intervention in glucose metabolism pathways, has emerged as a promising approach to enhance therapeutic outcomes.

The mechanism of tumor cell death plays a pivotal role in dictating neoplastic progression [21]. Cellular resistance to apoptosis, facilitated through diverse molecular pathways, represents a significant obstacle in cancer therapeutics. Pyroptosis, an increasingly recognized form of programmed inflammatory cell death governed by gasdermin (GSDM) protein family members, has emerged as a promising modality to increase immunotherapeutic efficacy [22–25]. This distinctive cell death process manifests through cytoplasmic expansion, culminating in membrane disruption, the subsequent release of cellular components, and the initiation of potent inflammatory cascades [26–28]. Contemporary research has shown increasing enthusiasm for harnessing nanobiotechnology and advanced nanomaterials to potentiate pyroptosis induction in malignant cells [29–31]. Current scientific exploration has identified several pyroptosis-inducing agents, including specific metal cations (notably Zn^{2+}, Sb^{3+}, and Co^{2+}) and reactive oxygen species (ROS) [32–37]. In parallel, tumor catalytic therapy has emerged as a promising therapeutic strategy, leveraging external stimuli or the TME to transform benign or minimally toxic endogenous compounds into potent cytotoxic molecules, particularly ROS, for selective tumor eradication [38–43]. Certain metal ions, including Fe^{2+}, Cu^{+}, and Mn^{2+}, demonstrate intrinsic enzyme-mimetic properties, enabling the catalysis of H_2O_2 within the TME to generate cytotoxic ROS, thereby facilitating microenvironment-targeted catalytic therapy [44–47]. Notably, Co-based nanozymes exhibit TME-activated cascade catalysis, efficiently transforming H_2O_2 into ROS, thereby facilitating the eradication of tumor cells [32,48]. However, the therapeutic potential of this approach is constrained by the inherently limited concentration of H_2O_2 within the tumor niche [49]. This limitation highlights the urgent necessity for the development of advanced catalytic systems that possess dual functionality: efficient conversion of H_2O_2 to ROS coupled with sustained amplification of H_2O_2 generation to maintain therapeutic efficacy.

The molecular cascade of GSDM-mediated pyroptosis initiates through mitochondrial impairment, leading to the liberation of mitochondrial DNA (mtDNA) [32,50]. This released mtDNA is facilitated to trigger the cyclic GMP-AMP synthase-stimulator of interferon gene (cGAS-STING) signaling axis, thereby potentiating antitumor immune activation [51–53]. The cGAS-STING pathway serves as a critical molecular switch in transforming immune-suppressed tumors into immune-responsive tumors, playing a central role in initiating and sustaining antitumor immunity [54–57]. Recent advancements in metalloimmunotherapy have revealed the immunoregulatory potential of various metal ions, including Mn^{2+}, Co^{2+}, Mg^{2+}, and Li^{+}, owing to their distinctive biological properties [19,58–63]. Among these, Co^{2+} has demonstrated the capacity to enhance STING activity in a cyclic GMP-AMP (cGAMP)-dependent manner, with no activation in the absence of cGAMP [32]. This specificity underscores the therapeutic potential of Co-based STING agonists in fine-tuning immune responses, particularly considering the pathological consequences of uncontrolled cGAS-STING pathway activation in inflammatory and degenerative disorders. However, NSUN2 (NOP2/Sun domain family, member 2) has emerged as a direct glucose sensor that is activated by glucose to suppress cGAS-STING signaling through TREX2 (three prime repair exonuclease 2) upregulation [15,64]. This mechanism drives oncogenesis and confers resistance to immunotherapeutic interventions. Therefore, the development of targeted strategies to induce tumor cell pyroptosis, coupled with the precise delivery of Co-containing nanoadjuvants, represents a critical approach for specific cGAS-STING pathway activation. Furthermore, therapeutic inhibition of tumor cell glycolysis has surfaced as a promising adjunct strategy to amplify STING activation, potentially enhancing immune system stimulation and improving therapeutic outcomes [15,65,66]. This multifaceted approach underscores the complex interplay between cellular metabolism, pyroptosis, and immune modulation in cancer therapy.

Herein, an innovative self-amplifying pyroptosis-STING nanoadjuvant, termed $GOCoF_2$ was developed and demonstrated significant therapeutic potential against HCC through dual modulation of tumor metabolism and the immunosuppressive microenvironment (Scheme 1). This nanoadjuvant was constructed by integrating glucose oxidase (GOx) onto the surface of cobalt fluoride (CoF_2) nanoenzymes, creating a sophisticated catalytic system. The $GOCoF_2$ nanoadjuvant exhibited a remarkable capacity for intratumoral H_2O_2 conversion into ROS, thereby initiating pyroptosis mechanisms. The unique self-sustaining feature of this system stemmed from its ability to deplete glucose while simultaneously generating additional H_2O_2, thus maintaining continuous catalytic activity. This metabolic manipulation, coupled with oxidative stress induction, significantly amplified cancer cell pyroptosis. The subsequent release of mtDNA activated the cGAS-STING pathway, with Co^{2+} acting as a synergistic enhancer. Notably, the glucose-dependent inhibition of TREX2 activity further potentiated the cGAS-STING pathway through metabolic regulation. This multifaceted approach elicited a robust immune response, resulting in substantial tumor growth suppression. When integrated with immune checkpoint blockade (ICB) therapy, $GOCoF_2$ demonstrated enhanced efficacy, effectively controlling both primary and distant tumor progression through systemic immune activation. Furthermore, a clinically relevant formulation was developed by incorporating $GOCoF_2$ into lipiodol embolic agents for TAE, yielding the $GOCoF_2$-lipiodol complex. This formulation showed superior efficacy in inhibiting orthotopic liver cancer in an experimental model. Our findings not only elucidated the intricate interplay between tumor metabolism and immune regulation but also provided a promising therapeutic paradigm for HCC. The $GOCoF_2$ nanoadjuvant represents a significant advancement in nanomedicine, offering a multifaceted approach to cancer therapy through simultaneous metabolic modulation and immune activation.

2. Results and discussion

2.1. Preparation and characterization of the $GOCoF_2$ nanoadjuvant

Initially, cobalt acetylacetonate and ammonium fluoride (NH_4F) were employed as sources of Co and F, respectively, to synthesize rod-shaped CoF_2 via high-temperature thermal synthesis. Subsequently, GOx self-assembled onto the surface of CoF_2 through DSPE-PEG_{2000}-NH_2 modification, leading to the formation of the $GOCoF_2$ nanoadjuvant (Fig. 1A). Transmission electron microscopy (TEM) analysis demonstrated the successful formation of well-defined rod-like CoF_2

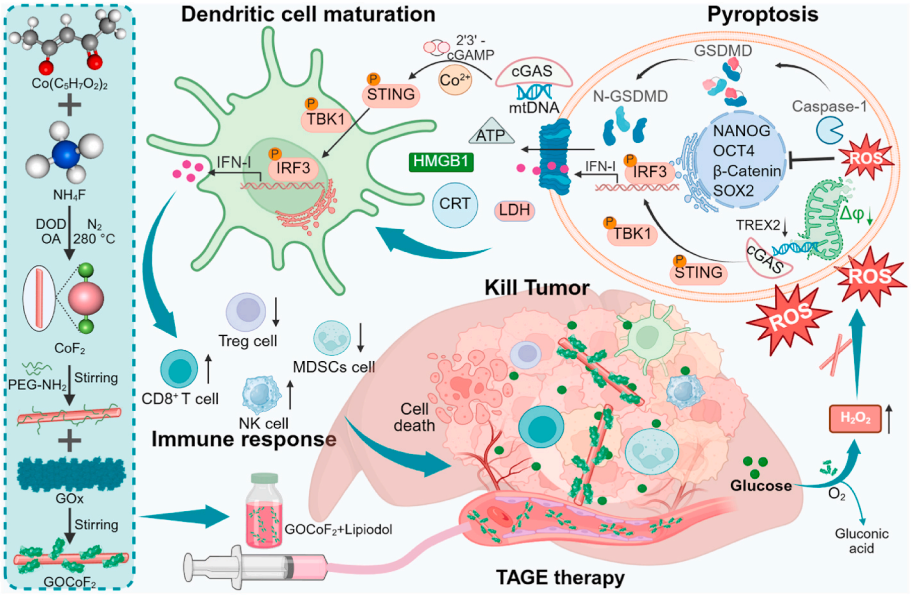

Scheme 1. Schematic illustration of self-reinforcing pyroptosis-STING nanoadjuvant driven by metabolic modulation for enhanced metalloimmunotherapy.

nanoparticles with a narrow size distribution, with typical dimensions of ~7.5 nm in width and ~200 nm in length (Fig. 1B, Fig. S1 and 2). Elemental mapping through energy dispersive X-ray spectroscopy (EDS) confirmed the homogeneous spatial distribution of Co and F within the nanostructures, verifying compositional uniformity (Fig. 1C). X-ray diffraction (XRD) patterns exhibited characteristic peaks corresponding to the tetragonal phase of CoF_2 (JCPDS 33–0417), confirming the presence of a crystalline structure (Fig. 1D). In addition, X-ray photoelectron spectroscopy (XPS) analysis revealed two distinct cobalt states with Co $2p_{3/2}$ and Co $2p_{1/2}$ binding energies of ~781.48 eV and ~797.88 eV, respectively, accompanied by characteristic shake-up satellite peaks at ~787.18 eV and ~803.38 eV (Fig. 1E, Fig. S3). The prominent F 1s signal at 684.18 eV further confirmed fluorine coordination with the metal centers through ionic bonding. These collective findings validated the successful synthesis of phase-pure CoF_2 nanorods via the high-temperature decomposition approach. The $GOCoF_2$ nanoadjuvant was successfully developed through surface modification with DSPE-PEG_{2000}-NH_2, thereby facilitating the integration of CoF_2 and GOx. UV–Vis spectral analysis revealed a distinctive GOx absorption signature in $GOCoF_2$ that was absent in bare CoF_2 nanoparticles (Fig. 1F). The successful immobilization of GOx on the CoF_2 nanozyme was further corroborated by zeta potential measurements and dynamic light scattering (DLS) analysis (Fig. 1G, Fig. S4). Moreover, Fourier transform infrared spectroscopy (FT-IR) characterization revealed vibrational modes in the 1500-1700 cm^{-1} range for $GOCoF_2$, which was remarkably consistent with the pure GOx spectra (Fig. 1H). To evaluate potential enzyme activity interference, comparative glucose depletion assays revealed equivalent glucose concentration reduction profiles for both free GOx and $GOCoF_2$ complexes, confirming preserved enzymatic functionality after nano-conjugation (Fig. S5). All these multidisciplinary characterizations collectively validated the successful fabrication of the $GOCoF_2$ nanoadjuvants, positioning them as promising therapeutic agents for oncological applications.

To systematically assess the catalytic properties of CoF_2 and $GOCoF_2$ nanoparticles under TME-mimetic conditions containing elevated glucose and H_2O_2 levels, we conducted a series of radical generation experiments. The oxygen radical production capacity was initially investigated using 1,3-diphenylisobenzofuran (DPBF) as a chromogenic indicator, where the characteristic absorption at 420 nm decreases proportionally with radical-mediated conversion to colorless 1,2-dibenzoylbenzene (DBB) (Fig. 1I). The time-dependent spectral analysis revealed significant DPBF degradation exclusively in the H_2O_2 + CoF_2 group, confirming efficient oxygen radical generation (Fig. 1J, Fig. S6). In addition, nitro blue tetrazolium (NBT) was further used to detect the generation of $O_2^{\bullet-}$. A time-dependent decrease in NBT absorbance was observed in the H_2O_2 + CoF_2 group, indicating that $O_2^{\bullet-}$ was effectively generated (Fig. 1K, Fig. S7). Subsequent evaluation of peroxidase-like activity through 3,5,3′,5′-tetramethylbenzidine (TMB) oxidation demonstrated marked ~652 nm absorbance enhancement in H_2O_2 + CoF_2 mixtures, indicative of effective hydroxyl radical (•OH) production (Fig. 1L–M, Fig. S8). In addition, o-phenylenediamine (OPD) was used to further identify the generation of •OH. The results showed that the characteristic peak intensity of OPD in the H_2O_2 + CoF_2 group increased significantly with time, further confirming •OH generation (Fig. 1N, Fig. S9). Furthermore, to validate the cascade catalytic activity of $GOCoF_2$, the DPBF probe was utilized to assess the ability of glucose to be enzymatically converted by GOx into H_2O_2, which was subsequently decomposed by CoF_2 into ROS. In the glucose + $GOCoF_2$ group, the absorbance of DPBF at about 420 nm was significantly reduced (Fig. 1O, Fig. S10). Similarly, the absorbance of NBT at about 260 nm was significantly reduced (Fig. 1P, Fig. S11). Further TMB oxidation experiments showed that only oxTMB was formed in the glucose + $GOCoF_2$ system (Fig. 1Q, Fig. S12). Similarly, only OPD in the glucose + $GOCoF_2$ group was oxidized (Fig. 1R, Fig. S13). These findings collectively demonstrated that the $GOCoF_2$ nanoadjuvant functions as self-amplifying biocatalysts, effectively utilizing TME-abundant glucose to elevate H_2O_2 concentrations and subsequently increase ROS (e.g., $O_2^{\bullet-}$, •OH) generation through catalytic reactions (Fig. 1S). This dual-substrate exploitation mechanism presented promising therapeutic potential for tumor-specific oxidative stress amplification.

2.2. *In vitro oxidative stress killing via $GOCoF_2$*

Given that the $GOCoF_2$ nanoadjuvant exhibited remarkable efficacy in terms of glucose consumption and ROS generation, we investigated its *in vitro* therapeutic effects and biological functions on H22 cells (Fig. 2A). First, the effects of GOx and $GOCoF_2$ on glucose metabolism in H22 cells were evaluated, as efficient cellular glucose consumption is essential for treatment efficacy. The results revealed that both the GOx and $GOCoF_2$ treatments caused significant glucose depletion in cancer cells after 12 h of incubation (Fig. 2B). Concurrently, CCK-8 assays revealed that GOx had a slight effect on cell viability, while both CoF_2

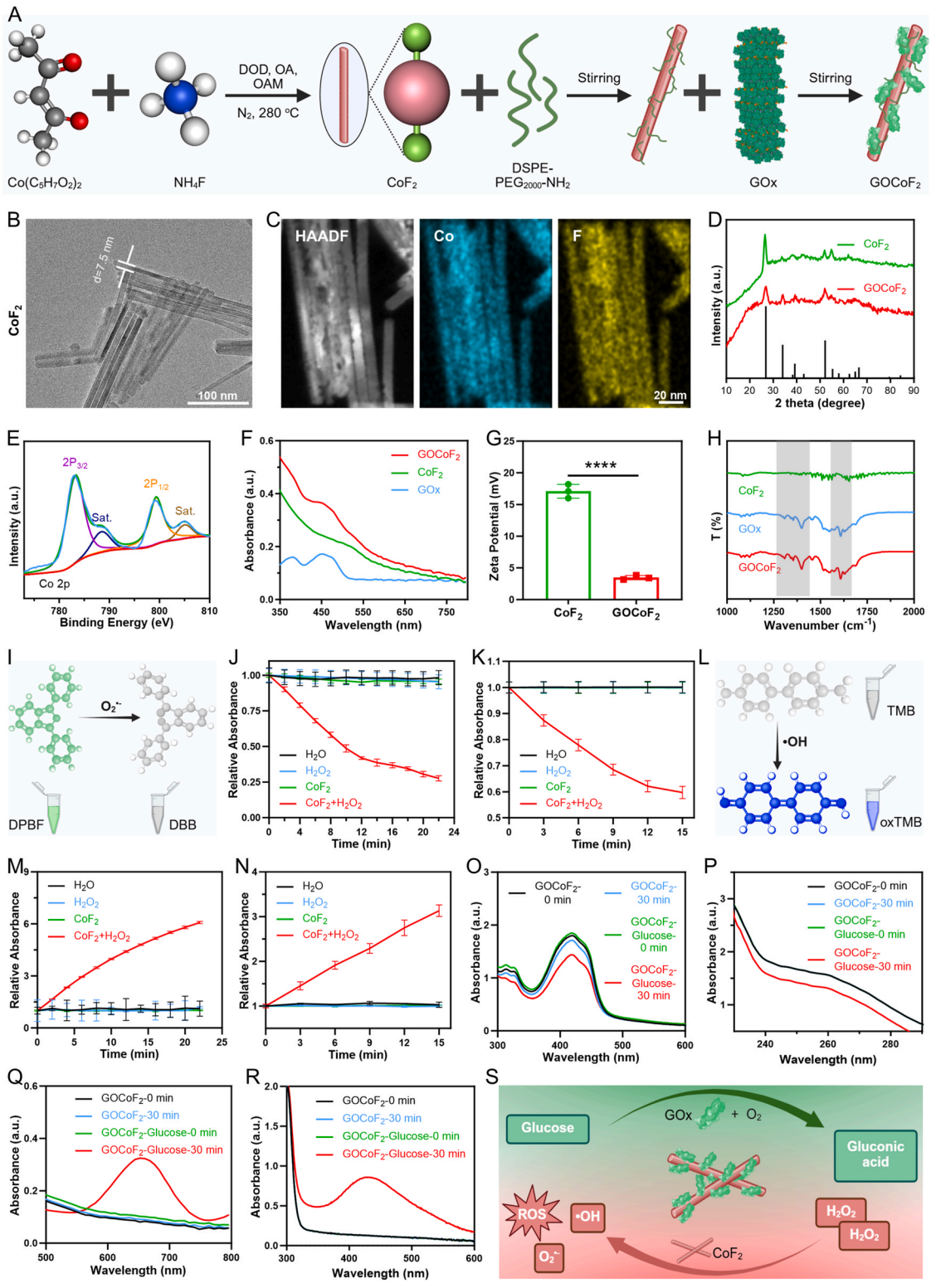

Fig. 1. Preparation and characterization of $GOCoF_2$. **A)** The synthetic process of $GOCoF_2$. **B)** TEM images of the CoF_2. **C)** HAADF-STEM image and CoF_2 element distribution (F, Co). **D)** XRD patterns of CoF_2 and $GOCoF_2$. **E)** XPS spectrum of Co 2p in CoF_2. **F)** UV–Vis spectra of GOx, CoF_2 and $GOCoF_2$. **G)** Zeta potentials of the CoF_2 and $GOCoF_2$. **H)** FT-IR spectra of GOx, CoF_2 and $GOCoF_2$. **I)** Diagram of the reaction of green DPBF with $O_2^{\bullet-}$ to form the colorless product DBB. **J)** Time-dependent oxidation of DPBF by the CoF_2 under H_2O_2. **K)** Time-dependent oxidation of NBT by the CoF_2 under H_2O_2. **L)** Schematic illustration of the TMB oxidation procedure. **M)** The TMB probe was used to study the time-dependent changes in the •OH generation efficiency of CoF_2 under H_2O_2. **N)** The OPD probe was used to study the time-dependent changes in the •OH generation efficiency of CoF_2 under H_2O_2. **O)** Time-dependent oxidation of DPBF by the $GOCoF_2$ under glucose. **P)** Time-dependent oxidation of NBT by the $GOCoF_2$ under glucose. **Q)** The time-dependent changes of •OH generation efficiency of the $GOCoF_2$ in the presence of glucose were investigated using a TMB probe. **R)** The time-dependent changes of •OH generation efficiency of the $GOCoF_2$ in the presence of glucose were investigated using a OPD probe. **S)** Schematic diagram of glucose catalysis by GOx to generate H_2O_2, which is then oxidized into ROS by CoF_2. The data are presented as the mean values ± SD. The P values indicated in the figure were determined by employing the two-tailed student's t-test. ****$p < 0.0001$.

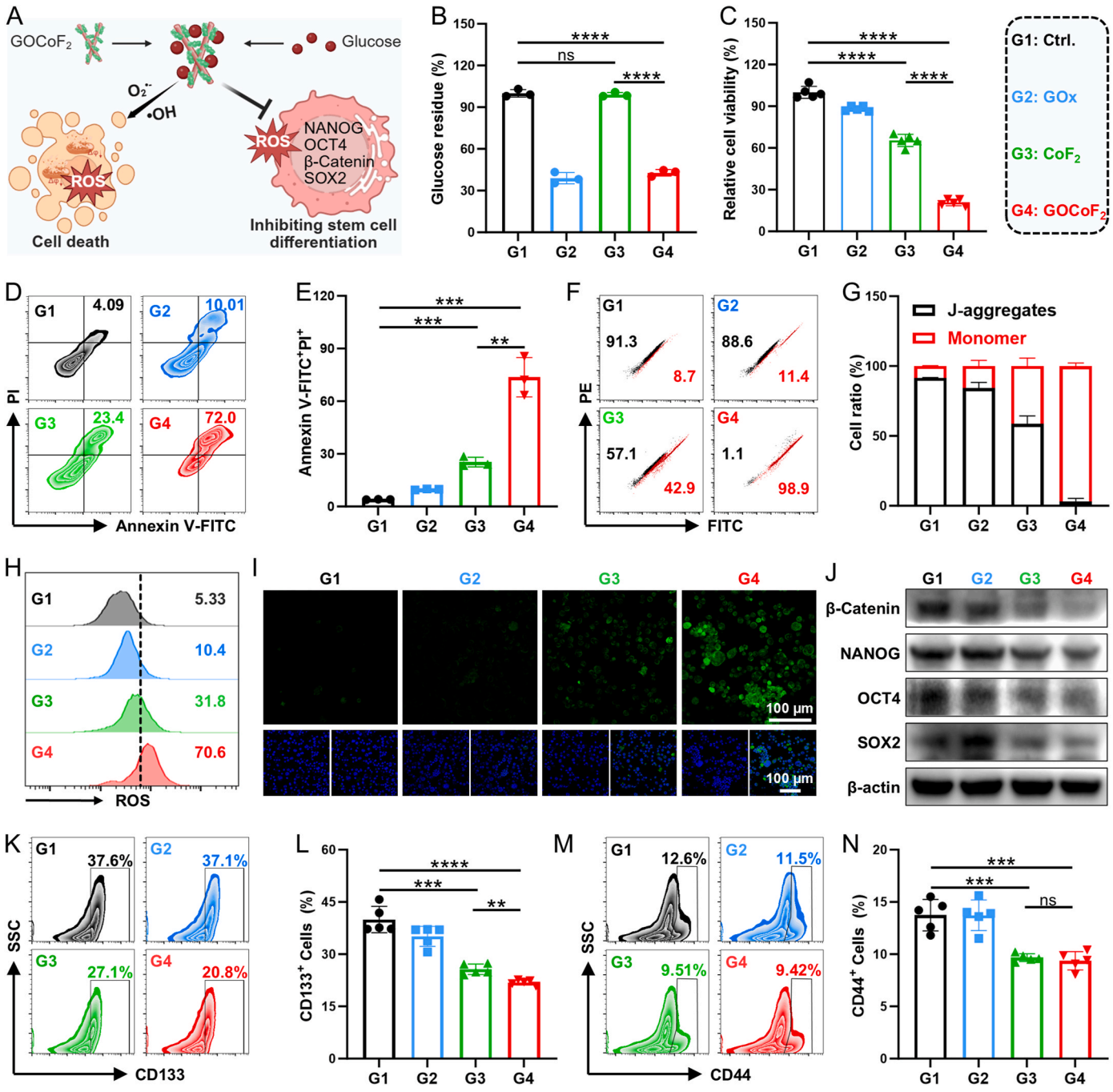

Fig. 2. ***In vitro*** **catalytic therapy by $GOCoF_2$. A)** Schematic diagram of the mechanism by which $GOCoF_2$ killed tumor cells and inhibited stemness by consuming glucose to produce ROS. **B)** Relative concentrations of glucose after various treatments. G1: Ctrl., G2: GOx, G3: CoF_2, G4: $GOCoF_2$. **C)** Relative viability of H22 cells after various treatments. **D)** Flow cytometry analysis and **E)** quantification of Annexin V-$FITC^+PI^+$ H22 cell after various treatments. **F)** Flow cytometry analysis and G) quantification of the mitochondrial membrane potential levels in H22 cells after various treatments. **H)** Flow cytometry analysis of ROS levels in H22 cells after various treatments. **I)** Confocal images of ROS-stained H22 cells after different treatments. **J)** The expression levels of β-catenin, NANOG, OCT4 and SOX2 in H22 cells were detected by western blotting. **K)** Flow cytometry analysis and **L)** quantification of $CD133^+$ H22 cells after different treatments. **M)** Flow cytometry analysis and **K)** quantification of $CD44^+$ H22 cells after different treatments. The data are presented as the mean values ± SD. The P values indicated in the figure were determined by employing the two-tailed student's t-test. $^{**}p < 0.01$, $^{***}p < 0.001$, $^{****}p < 0.0001$.

and $GOCoF_2$ markedly decreased cell viability. Notably, $GOCoF_2$ demonstrated a more pronounced effect compared with CoF_2 (Fig. 2C). To further investigate the cytotoxic effects of $GOCoF_2$ on H22 cells, we employed Annexin V-FITC and PI staining in conjunction with flow cytometry analysis. The results indicated that $GOCoF_2$ treatment significantly induced H22 cell death (Fig. 2D and E). The evaluation of mitochondrial dysfunction via the JC-1 probe revealed a substantial increase in the proportion of depolarized mitochondria (monomer/aggregate ratio) following $GOCoF_2$ exposure (Fig. 2F and G). Specifically, the monomer ratio in H22 cells increased from approximately 8.7 %–42.9 % after CoF_2 treatment, while $GOCoF_2$ treatment markedly elevated this ratio to approximately 98.9 %. To further investigate the altered state of oxidative stress in H22 cells, a 2′,7′-dichlorodihydrofluorescein diacetate (DCFH-DA) probe was employed to quantify intracellular ROS generation. Flow cytometric analysis demonstrated a significant elevation in intracellular ROS levels following $GOCoF_2$

treatment (Fig. 2H, Fig. S14). Consistent with these findings, confocal microscopy revealed greater green fluorescence intensity in the $GOCoF_2$-treated cells than in the modest signal observed in CoF_2-treated cells, confirming robust intracellular ROS generation (Fig. 2I, Fig. S15). Together, these findings suggested a cascade pathway from metabolic disruption to oxidative stress-induced cell death. The aerobic glycolysis of cancer, also known as the Warburg effect, represents a critical metabolic hallmark of malignancy. This phenomenon is intricately associated with the maintenance of cancer stem cell characteristics, tumor progression, metastasis, and chemoresistance. Consequently, we conducted an in-depth evaluation of the impact of this strategy on tumor stemness. Notably, after 24 h of co-incubation of H22 cells with $GOCoF_2$, Western blot analysis revealed significant downregulation of the expression of stemness markers, such as β-catenin, NANOG, OCT4, and SOX2 (Fig. 2J). Furthermore, flow cytometry analysis revealed a substantial decrease in the expression of the stem cell markers CD133 and CD44 in H22 cells (Fig. 2K–N), which suggested the inhibition of tumor stem-like properties. These findings collectively demonstrated that the $GOCoF_2$ nanoadjuvant exhibited potent antitumor activity through metabolic modulation (specifically glucose depletion), ROS-mediated cellular damage, and the inhibition of stemness, which showed considerable promise for the development of novel metabolic intervention strategies against HCC.

2.3. Activation and amplification of the self-cascading pyroptosis and cGAS-STING pathway

Considering the potential for ROS accumulation in the cellular environment and $GOCoF_2$-mediated biological effects, which can synergistically induce inflammatory pathways and pyroptosis, we performed a more comprehensive analysis of the mechanisms of cell death. Initial assessment of H22 cell morphology was performed through Annexin V-FITC/PI dual fluorescence labeling, an established method for detecting alterations in membrane integrity. The staining mechanism relies on annexin V binding to externalized phosphatidylserine- and PI-stained nuclei in permeabilized cells. Confocal imaging revealed distinctive membrane blebbing, a key morphological indicator of pyroptosis in $GOCoF_2$-treated H22 cells (Fig. 3A). Cell pyroptosis is a sophisticated form of programmed cell death that amplifies antitumor immunity via the liberation of proinflammatory intracellular components and tumor-associated antigens. Comparative analysis revealed a marked increase in adenosine triphosphate (ATP) and lactate dehydrogenase (LDH) secretion from H22 cells in the $GOCoF_2$-treated group compared with the CoF_2 group (Fig. 3B and C). In addition, $GOCoF_2$-triggered pyroptosis significantly enhanced the secretion of the inflammatory cytokine interleukin (IL)-1β (Fig. 3D). Subsequent investigations were conducted to corroborate the immunogenic cell death (ICD) mechanism associated with pyroptosis induction. Flow cytometric analysis revealed enhanced calreticulin (CRT) expression in H22 cells subjected to the $GOCoF_2$ nanoadjuvant, indicating successful CRT externalization (Fig. 3E and F). Concurrently, the nuclear high mobility group box 1 (HMGB1) content in the $GOCoF_2$-treated cells was substantially reduced (Fig. 3G and H). These findings confirmed that $GOCoF_2$ administration markedly augmented oxidative stress, culminating in pyroptosis. Biological TEM further substantiated these observations, revealing pronounced cell ultrastructural alterations, including mitochondrial dilation, cristae obliteration, and vacuole formation (Fig. 3I). To further elucidate the molecular mechanisms underlying pyroptosis induction, Western blot analysis was conducted to evaluate the expression profiles of key pyroptosis-associated proteins in $GOCoF_2$-treated cells. The quantitative assessment revealed significant upregulation of cleaved Caspase-1 (C-Caspase-1) and N-GSDMD, which were pivotal mediators of the canonical pyroptosis pathway, in response to $GOCoF_2$ exposure (Fig. 3J). Mechanistically, activated C-Caspase-1 catalyzes the proteolytic cleavage of GSDMD proteins, leading to the formation of N-terminal oligomers that perforate the plasma membrane. This membrane permeabilization facilitates the release of cytoplasmic contents, ultimately executing the pyroptosis program. Collectively, these results demonstrated that $GOCoF_2$ triggered substantial pyroptosis activation through a sequential mechanism involving glucose deprivation and ROS accumulation.

To investigate the consequential effects of ROS-mediated DNA damage, a comet assay analysis was performed, and the results demonstrated that $GOCoF_2$-treated H22 cells presented substantially elongated tail moments compared with control and CoF_2-treated groups (Fig. 3K). However, NSUN2 functions as a direct glucose sensor that is activated by glucose to suppress cGAS-STING signaling via the upregulation of TREX2 [64]. This mechanism promotes oncogenesis and confers resistance to immunotherapeutic interventions. Western blot analysis confirmed a significant reduction in TREX2 expression following GOx and $GOCoF_2$ exposure (Fig. 3L, Fig. S16), indicating that $GOCoF_2$-mediated glucose depletion disrupts TREX2 methylation, consequently promoting dsDNA accumulation and cGAS-STING signaling. Pyroptosis facilitates the release of extensive mtDNA release, which serves as a potent cGAS-STING activator [50]. Given the well-established role of Co^{2+} in amplifying cGAMP-dependent STING activity, we hypothesized that $GOCoF_2$ functioned as a specific STING agonist. To validate this hypothesis, we assessed cGAS-STING pathway activation and observed a significant increase in the levels of phosphorylated TBK1, IRF3, and STING (p-TBK1, p-IRF3, and p-STING) proteins under both CoF_2 and $GOCoF_2$ conditions, with marked superiority in the $GOCoF_2$ group (Fig. 3M). These findings underscored the pivotal role of $GOCoF_2$ in modulating the glucose metabolism cascade, thereby activating the pyroptosis-STING pathway. The proposed mechanism by which $GOCoF_2$ mediated cell pyroptosis and STING pathway activation could be outlined as follows (Fig. 3N). Initially, $GOCoF_2$ triggered an intracellular glucose cascade that increased ROS generation. This ROS surge activated Caspase-1, which cleaved GSDMD into its N-terminal fragments. These cleaved fragments subsequently translocated to the plasma membrane, where they formed transmembrane pores that enabled the release of intracellular components. This process not only induced pyroptosis but also caused DNA damage in tumor cells through ROS-mediated pathways. Simultaneously, the liberated cellular components, particularly mtDNA, acted as molecular signals detected by cGAS. This recognition initiated and amplified the cGAS-STING signaling cascade. Through this dual mechanism, $GOCoF_2$ exerted its antitumor effects by regulating glucose metabolism and stimulating the pyroptosis-STING signaling axis. This coordinated action effectively reversed the immunosuppressive TME and augmented antitumor immune responses, thereby enhancing therapeutic outcomes.

2.4. In vivo antitumor study and immune evaluation mediated by $GOCoF_2$

To explore the remarkable cytotoxic activity of $GOCoF_2$ against H22 tumor cells *in vitro*, we investigated its therapeutic potential in vivo. Following tumor establishment (volume ~150 mm^3), H22 tumor-bearing mice were randomized into four cohorts: (1) untreated control, (2) GOx, (3) CoF_2, and (4) $GOCoF_2$. On day 0, the respective groups received intratumoral injections of GOx, CoF_2, or $GOCoF_2$, and the therapeutic outcomes were monitored every other day (Fig. 4A). Quantitative tumor volume analysis demonstrated that while GOx alone provided moderate tumor suppression, both CoF_2 and $GOCoF_2$ treatments significantly impaired tumor progression, with $GOCoF_2$ exhibiting superior anti-tumor activity (Fig. 4B, Fig. S17). These results indicated that the $GOCoF_2$ nanoadjuvant could effectively manipulate tumor glucose metabolism to potentiate cancer treatment. Notably, the $GOCoF_2$ group exhibited significantly increased long-term survival, as all five mice achieved complete tumor eradication and remained tumor-free for more than 30 days (Fig. 4C). All treatment regimens were well-tolerated, as evidenced by stable body weights throughout the study (Fig. S18). In addition, hematoxylin and eosin (H&E) staining of major organs from $GOCoF_2$ treated mice revealed no obvious damage or

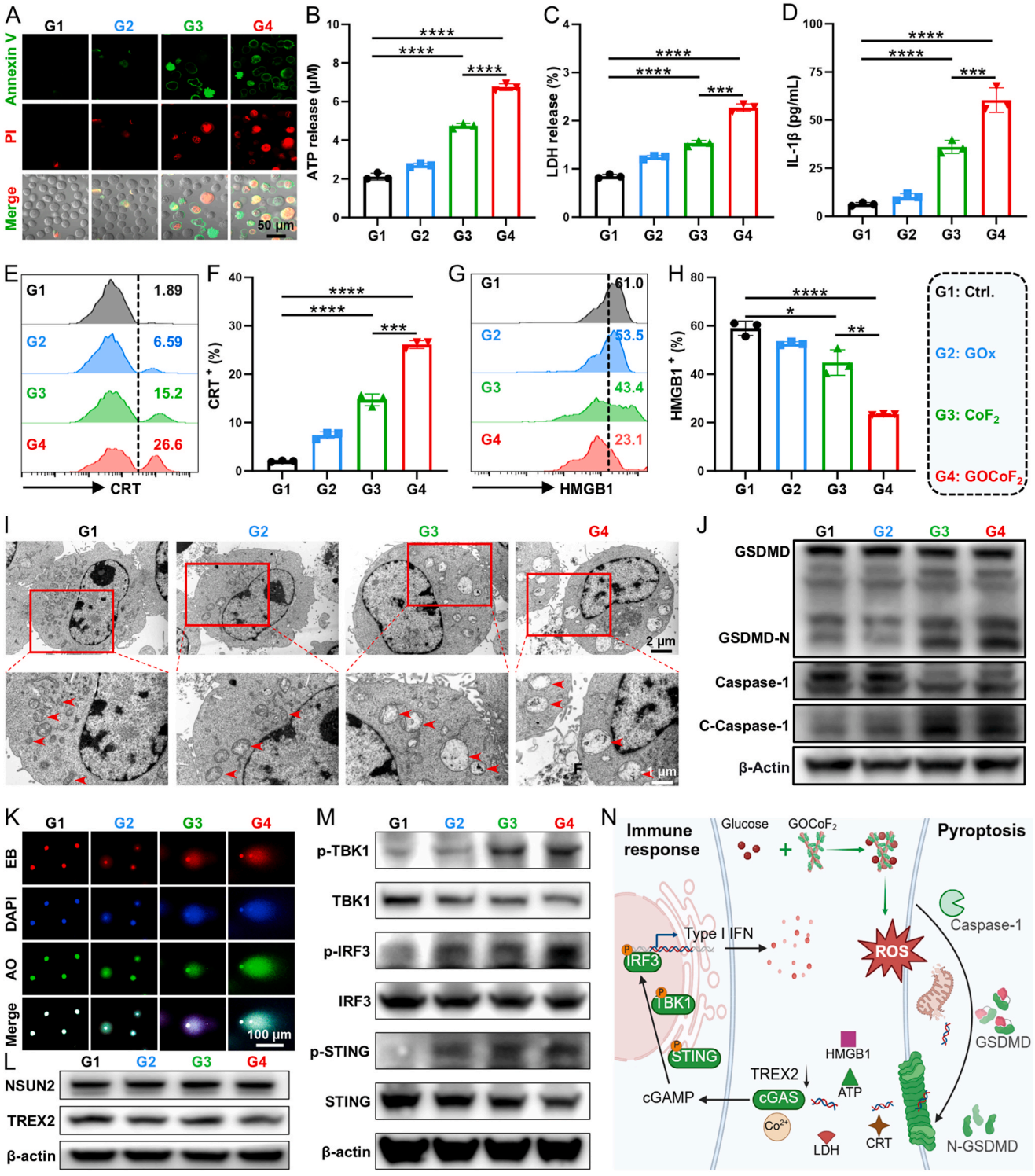

Fig. 3. Activation and amplification of the self-cascading pyroptosis and cGAS-STING pathway. A) Confocal fluorescence images showing pyroptosis in H22 cells after different treatments. G1: Ctrl., G2: GOx, G3: CoF_2, G4: $GOCoF_2$. **B)** ATP release by H22 cells after different treatments. **C)** LDH release levels in H22 cells after different treatments. **D)** Secretion levels of IL-1β from H22 cells after different treatments detected by ELISA. **E)** Flow cytometry analysis and **F)** quantification of CRT expression in H22 cells after various treatments. **G)** Flow cytometry analysis and **H)** quantification of HMGB1 release in H22 cells after various treatments. **I)** Biological TEM images showing the mitochondria of H22 cells after different treatments. **J)** The expression levels of GSDMD, Caspase-1, GSDMD-N, and C-Caspase-1 in H22 cells were detected via western blotting analysis. **K)** Comet assay images showing the DNA damage in H22 cells after different treatments. EB: Ethidium Bromide, AO: Acridine Orange. **L)** The expression levels of NSUN2 and TREX2 in H22 cells after different treatments were detected by Western blot analysis. **M)** The expression levels of p-TBK1, TBK1, p-IRF3, IRF3, p-STING, and STING in H22 cells were detected via western blotting analysis. **N)** The diagram illustrated that $GOCoF_2$ induced tumor cell pyroptosis by consuming glucose to produce ROS and cascade to activate the STING pathway. The data are presented as the mean values ± SD. The P values indicated in the figure were determined by employing the two-tailed student's t-test. *p < 0.05, **p < 0.01, ***p < 0.001, ****p < 0.0001.

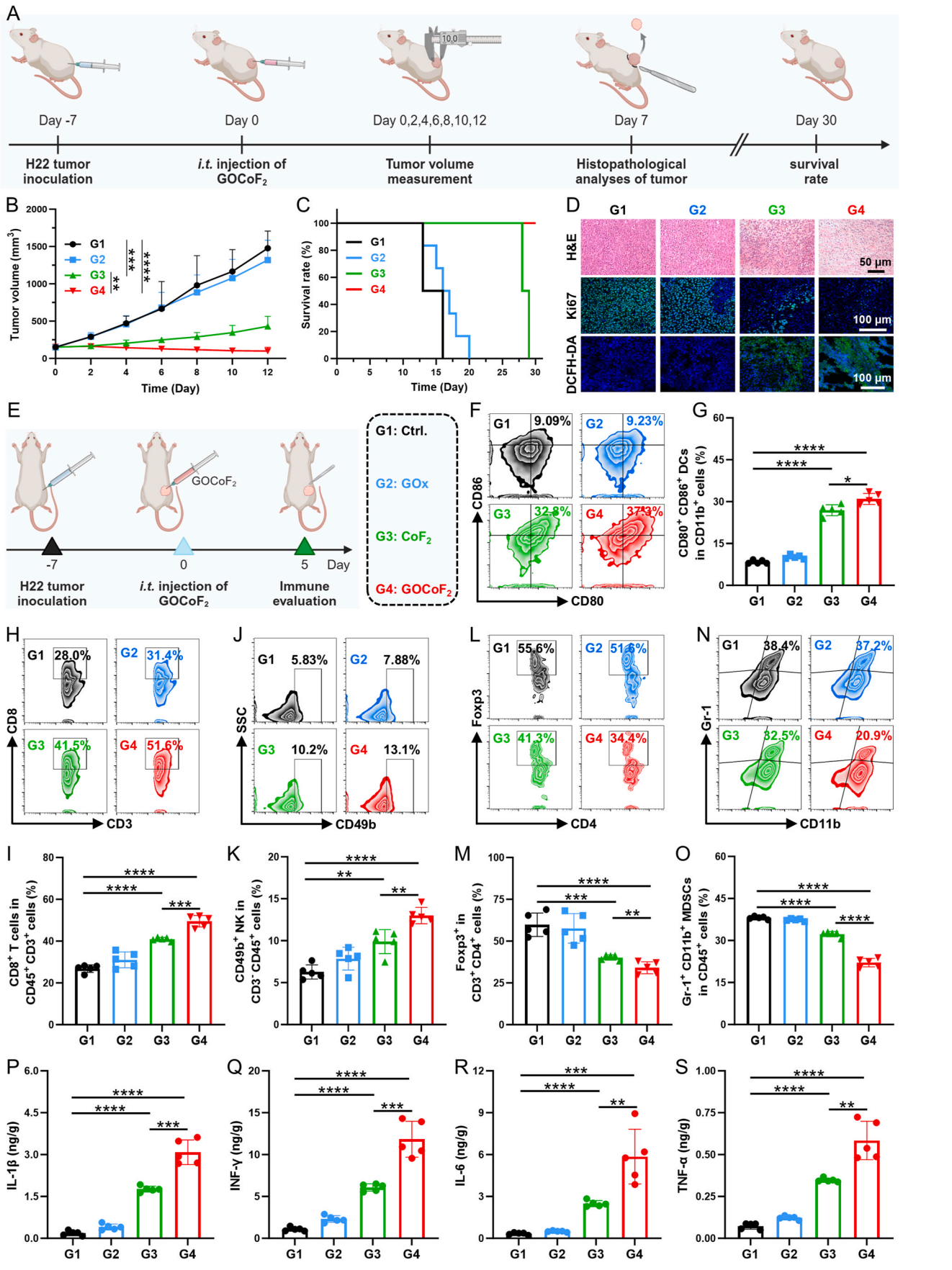

(caption on next page)

Fig. 4. In vivo antitumor study and immune evaluation mediated by $GOCoF_2$. A) Schematic illustration of the in vivo treatment procedure in mice. **B)** Changes in the tumor growth curve after different treatments. G1: Ctrl., G2: GOx, G3: CoF_2, G4: $GOCoF_2$. **C)** Survival rate curves of the mice after different treatments for 30 days. **D)** Images of tumor sections after H&E, Ki-67, and DCFH-DA staining obtained from mice subjected to different treatments. **E)** Schematic illustration of the in vivo treatment procedure in mice. **F)** Flow cytometry analysis of $CD80^+$ $CD86^+$ matured DCs among $CD11c^+$ cells within the lymph node after different treatments and **G)** statistical data. **H)** Flow cytometry analysis of $CD8^+$ T cells among $CD3^+$ $CD45^+$ cells and **I)** quantitative analysis. **J)** Flow cytometry analysis of $CD49b^+$ NK cells among $CD3^-$ $CD45^+$ T cells and **K)** quantitative analysis. **L)** Flow cytometry analysis of $Foxp3^+$ Tregs among $CD3^+$ $CD4^+$ T cells and **M)** quantitative analysis. **N)** Flow cytometry analysis of $Gr\text{-}1^+$ $CD11b^+$ MDSCs among $CD45^+$ T cells and **O)** quantitative analysis. **P-S)** The concentrations of IL-1β, IFN-γ, IL-6 and TNF-α in the supernatant after various treatments. The data are presented as the mean values ± SD. The P values indicated in the figure were determined by employing the two-tailed student's t-test. *$p < 0.05$, **$p < 0.01$, ***$p < 0.001$, ****$p < 0.0001$.

inflammation, indicating the excellent biocompatibility of this therapeutic strategy (Fig. S19). Moreover, the serum biochemical analysis revealed that all the parameters in the $GOCoF_2$-treated mice remained within normal ranges and were not significantly different from those in the control group, confirming the absence of significant toxic effects (Fig. S20). To investigate the underlying mechanisms of $GOCoF_2$-induced tumor regression, H&E staining revealed extensive cellular damage in the $GOCoF_2$-treated tumors, characterized by pronounced cellular shrinkage and nuclear loss (Fig. 4D). Complementary Ki67 immunofluorescence analysis confirmed significant suppression of cellular proliferation in the $GOCoF_2$ group, indicating reduced tumor aggressiveness (Fig. 4D, Fig. S21). To further investigate the mechanism, tumor sections were subjected to ROS staining. Compared with those in the control group, the CoF_2-treated tumors displayed green fluorescence, while the $GOCoF_2$ group exhibited markedly stronger fluorescence intensity (Fig. 4D, Fig. S22). Collectively, these findings demonstrated that $GOCoF_2$ effectively alleviated the tumor burden and improved survival outcomes, suggesting a novel therapeutic paradigm for solid tumor management.

The ultimate objective of tumor therapy extends beyond localized tumor eradication, encompassing systemic immune activation to counteract the immunosuppressive TME, thereby preventing tumor metastasis and recurrence. To delineate the mechanisms underlying its enhanced therapeutic performance, we performed detailed investigations into its antitumor immune effects. Following a 5-day treatment regimen, tumor tissues and associated lymph nodes were harvested and homogenized for immunological profiling (Fig. 4E). Flow cytometric evaluation of dendritic cell (DC) maturation in the lymph nodes revealed that both CoF_2 and $GOCoF_2$ treatments outperformed other interventions in stimulating DC maturation, with $GOCoF_2$-treated mice showing markedly elevated populations of mature DCs within tumors (Fig. 4F and G). This enhancement was pivotal for optimizing subsequent antigen presentation processes. Further examination of T-cell dynamics in the TME revealed a substantial increase in the proportion of $CD8^+$ cytotoxic T lymphocytes post-treatment with CoF_2 or $GOCoF_2$, which was particularly pronounced in the $GOCoF_2$-treated group (Fig. 4H and I), underscoring the robust induction of antitumor immunity. $GOCoF_2$ also notably augmented the infiltration of natural killer (NK) cells into tumor sites (Fig. 4J and K), reinforcing its therapeutic potency. Consistent with these findings, $GOCoF_2$ treatment led to a reduction in regulatory T cells (Tregs) and myeloid-derived suppressor cells (MDSCs) (Fig. 4L–O). The diminished presence of these immunosuppressive entities validated the successful mobilization of antitumor defenses, potentially improving immunotherapeutic outcomes. Moreover, cytokine profile alterations were quantified via enzyme-linked immunosorbent assay (ELISA). The $GOCoF_2$ administration resulted in a significant increase in the level of interleukin IL-1β, a critical mediator in the pyroptosis pathway (Fig. 4P), alongside elevated levels of cytotoxic cytokines such as interferon-γ (IFN-γ), IL-6, and tumor necrosis factor-α (TNF-α) (Fig. 4Q–S). Above all, $GOCoF_2$ orchestrated a tumor glucose-fuelled pyroptosis sequence, fostering immune cell infiltration and increasing proinflammatory cytokine release, culminating in a fortified antitumor immune response.

2.5. RNA sequencing and analysis of the therapeutic mechanism

To better understand the underlying therapeutic mechanisms of the $GOCoF_2$ nanoadjuvant in HCC, we performed transcriptomic profiling to analyze mRNA expression changes in H22 tumor tissues before and after treatment. Unsupervised hierarchical clustering revealed distinct groupings of samples within the same treatment cohort, underscoring the reliability of the RNA sequencing data (Fig. S23). Comparative analysis revealed 887 differentially expressed genes (DEGs) between the $GOCoF_2$-treated and control groups, including 216 downregulated and 671 upregulated genes (Fig. 5A–C). To further explore the biological significance of these DEGs, gene ontology (GO) and Kyoto Encyclopedia of Genes and Genomes (KEGG) pathway analyses were conducted, revealing functional annotations and pathway enrichments associated with the observed mRNA changes (Fig. 5D). KEGG pathway enrichment analysis revealed that the DEGs identified after $GOCoF_2$ treatment were predominantly involved in inflammatory and stress-responsive pathways, such as the NF-κB, cytokine-cytokine receptor interaction, Toll-like receptor, IL-17, TNF, MAPK, NOD-like receptor, FoxO, p53, JAK-STAT, reactive oxygen species, and PI3K-Akt signaling pathways (Fig. 5E). These findings suggested a strong link between $GOCoF_2$-induced inflammation, driven by tumor glucose utilization, and oxidative stress-mediated pyroptosis. Intriguingly, metabolic pathways and the HIF-1 signaling pathway were also significantly enriched, indicating potential shifts in tumor energy metabolism and oxygen homeostasis following treatment (Fig. 5E). To further dissect the key regulatory genes within these pathways, a chord diagram was constructed via KEGG analysis, revealing that the most prominently regulated genes were associated with cytokine-cytokine receptor interactions, the MAPK signaling pathway, the PI3K-Akt signaling, and the HIF-1 signaling pathway (Fig. 5F). To further explore the changes and alterations in $GOCoF_2$ and genes related to glucose metabolism, cell pyroptosis, the immune response, and stemness. We performed gene set enrichment analysis (GSEA), and the results revealed that genes related to the glucose metabolic process and cell pyroptosis were significantly upregulated in tumor tissues (Fig. 5G and H). It is worth noting that in tumors treated with $GOCoF_2$, genes involved in the activation of innate immune response pathway and the adaptive immune response pathway, which are closely related to the STING pathway, were significantly upregulated (Fig. 5I, Fig. S24). This finding further verified that $GOCoF_2$ induced a strong immune response to kill tumors. In addition, genes related to the negative regulation of stem cell proliferation pathway related to stemness were all upregulated (Fig. 5J), confirming that $GOCoF_2$ inhibited tumor stem-like properties. Collectively, these transcriptomic findings underscored the multifaceted role of $GOCoF_2$ in modulating tumor glucose metabolism and inducing pyroptosis, thereby highlighting its therapeutic potential in anti-tumor strategies. Overall, RNA sequencing provided a comprehensive view of the transcriptional alterations induced by $GOCoF_2$ in tumor tissues. These results not only confirmed the central role of $GOCoF_2$ in regulating glucose metabolism but also revealed its ability to activate inflammatory and stress-related pathways, ultimately leading to pyroptosis. These findings further solidified the therapeutic efficacy of $GOCoF_2$ in targeting tumor cells through metabolic and immune modulation, offering a promising avenue for cancer treatment.

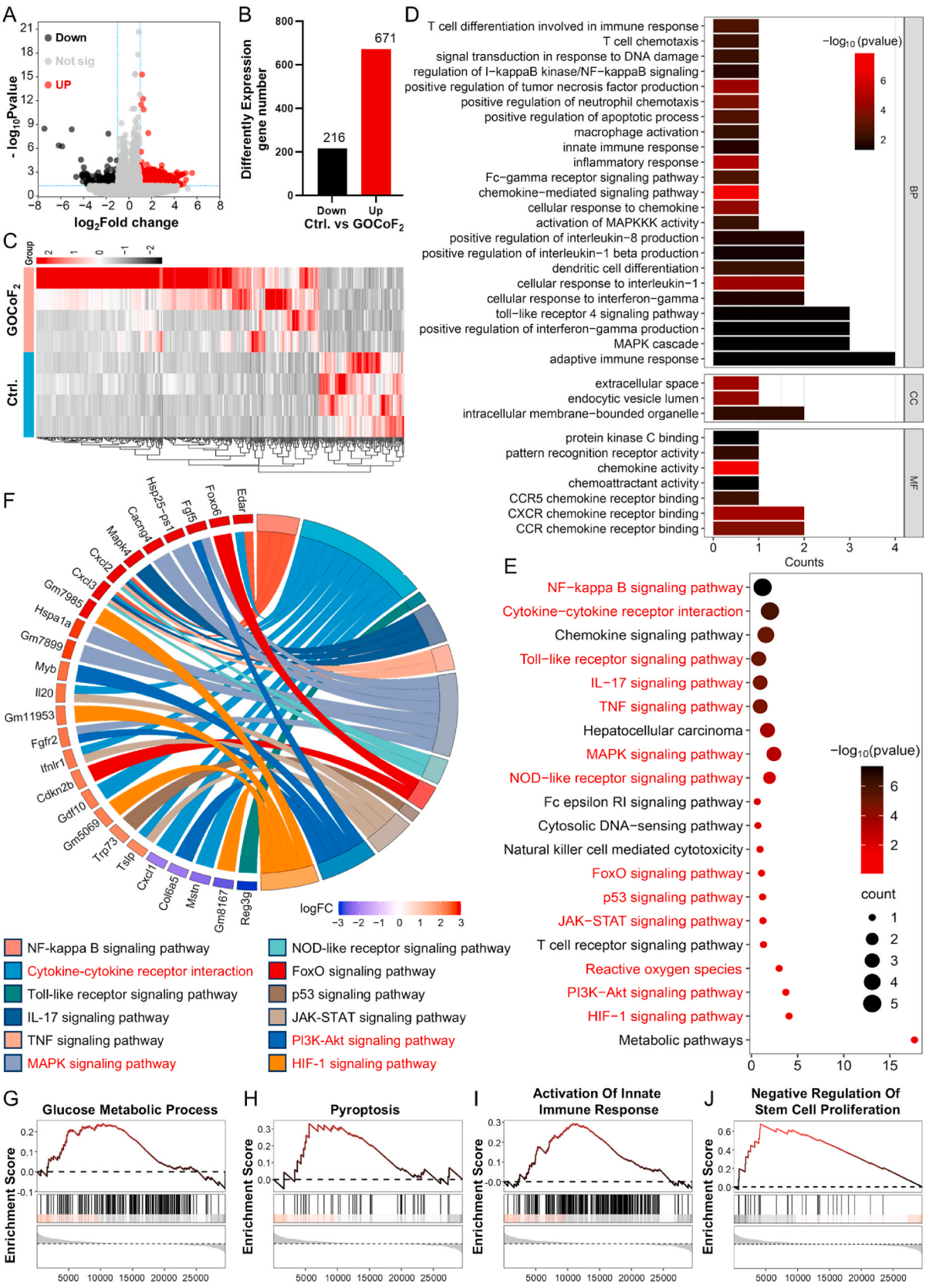

Fig. 5. Transcriptional analysis of H22 subcutaneous tumors after various treatments was performed by RNA-seq. A) Volcano plots and **B)** numbers of the downregulated genes and upregulated genes in the $GOCoF_2$ group compared with the control group. **C)** Cluster diagram of DEGs between the of $GOCoF_2$ group and the control group (n = 4 per group). **D)** GO and KEGG analyses of the differentially expressed genes in the $GOCoF_2$ group and control group (BP, biological process; CC, cellular component; MF, molecular function). **E)** KEGG enrichment analysis for studying underlying pathways after $GOCoF_2$ treatments. **F)** Circle diagram of KEGG enrichment analysis of inflammation/immune-related DEGs. **G-J)** GSEA analysis showed the gene sets of Glucose Metabolic Process, Pyroptosis, Activation of Iinnate Immune Response and Negative Regulation of Stem Cell Proliferation signaling pathway.

2.6. Treatment of bilateral tumors with the combination of $GOCoF_2$ and α-PD-1 therapy

Despite the remarkable therapeutic potential of ICB in cancer immunotherapy, its clinical effectiveness is frequently limited by the immunosuppressive TME [67–70]. Nevertheless, the profound immunosuppressive milieu characteristic of HCC frequently compromises therapeutic outcomes. In this context, pyroptosis engineering has emerged as a promising avenue to potentiate immune activation and enhance therapeutic responses. Given the demonstrated efficacy of $GOCoF_2$, subsequent investigations focused on evaluating its systemic anticancer properties when combined with α-PD-1 blockade. In this study, H22 cell tumor-bearing mice with bilateral lesions were divided into four experimental cohorts. The right-sided tumor served as the primary treatment target, while the left-sided lesion remained untreated to model distant metastasis. The experimental design comprised: (1) control, (2) α-PD-1, (3) $GOCoF_2$, and (4) $GOCoF_2$ combined with α-PD-1. On day 0, primary tumors in groups 3 and 4 received $GOCoF_2$ injection, followed by systemic α-PD-1 administration on days 1, 4, and 7 for groups 2 and 4 (Fig. 6A). The combination therapy demonstrated superior efficacy in primary tumor management, achieving complete tumor regression in approximately 40 % of the mice, underscoring the therapeutic superiority of this dual-modality approach (Fig. 6B and C, Fig. S25). Notably, local $GOCoF_2$ application independently reduced distant tumor progression, with enhanced anti-tumor effects observed when $GOCoF_2$ was combined with α-PD-1 (Fig. 6D and E, Fig. S26). The treatment response was further corroborated by significant reductions in both primary and distal tumor weights following combination therapy (Fig. 6F and G). Complementary immunofluorescence analysis of tumor sections revealed increased $CD45^+$ and $CD8^+$ infiltration in the combination therapy group, suggesting increased immune activation (Fig. 6H and I, Fig. S27 and 28). Throughout the treatment course, maintained body weights confirmed the safety profile of this therapeutic regimen (Fig. S29). These findings collectively demonstrated that the integration of $GOCoF_2$-mediated catalytic metalloimmunotherapy with ICB potentiated systemic anti-tumor immunity, effectively controlling both primary and metastatic lesions through a self-amplified pyroptosis-STING activation pathway.

2.7. $GOCoF_2$-mediated embolization of rat orthotopic N1S1 HCC tumors

TAE and TACE are recognized as primary therapeutic approaches for treating HCC who are not amenable to surgical resection [3]. In TACE procedures, therapeutic agents, including chemotherapeutic drugs and embolic materials such as lipiodol or polymeric microspheres, are selectively delivered into the hepatic artery to occlude the hepatic tumor. However, this therapeutic strategy is significantly impeded by the immunosuppressive characteristics of the TME, which markedly diminishes treatment effectiveness [71]. Given that our developed $GOCoF_2$ nanoadjuvant demonstrated exceptional capabilities in reprogramming the immunosuppressive TME during combined immunotherapeutic approaches in murine models, we subsequently developed a combined therapeutic approach by incorporating $GOCoF_2$ into lipiodol-based TAE (TAGE) treatment (Fig. 7A). The TAGE emulsion ($V_{Lipiodol}$: $V_{Aqueous}$ = 2:1) was obtained by mixing and stirring the $GOCoF_2$ aqueous solution with lipiodol (Fig. 7B). The experimental investigation employed orthotopic HCC models in rats, in which N1S1 tumor cells were stereotactically implanted into the left hepatic lobe. 7 days after tumor cell implantation, the experimental subjects were allocated into three treatment groups: Group I (control), Group II (TAE with lipiodol alone), and Group III (TAGE with lipiodol incorporating $GOCoF_2$). Longitudinal tumor monitoring via a 7.0 T small animal MRI system at 0, 4, 7, and 14 days post-intervention revealed differential therapeutic responses across treatment groups. While Lipiodol-based TAE partially suppressed N1S1 tumor progression relative to that of untreated controls, the TAGE of $GOCoF_2$ significantly augmented this antitumor effect (Fig. 7C–E). Complementary histological evaluation of N1S1 tumor specimens harvested on days 7 post-treatment through H&E and Ki67 staining confirmed these findings. The tissue sections from the rats that received Lipiodol combined with $GOCoF_2$ presented the most extensive tumor necrosis and the lowest cellular proliferation indices (Fig. 7F, Fig. S30). Further characterization through immunofluorescence assays demonstrated enhanced immune cell infiltration, as indicated by increased $CD45^+$ cell populations in tumors treated with the TAGE therapies (Fig. 7G, Fig. S31). This immunological remodeling of the TME suggested a potential mechanism underlying the observed therapeutic enhancement. Collectively, these findings established the translational potential of $GOCoF_2$, not only as an intratumoral therapeutic agent but also as an effective adjunct in TAE/TACE-based locoregional therapies for hepatic malignancies.

3. Conclusion

In summary, the innovative $GOCoF_2$ nanoplatform was constructed to introduce a transformative approach to simultaneously address tumor metabolic adaptation and the immunosuppressive microenvironment in HCC treatment. This self-amplifying nanoadjuvant, engineered through the integration of GOx with CoF_2 nanozymes, created a tumor-selective catalytic cycle that disrupted glycolytic pathways and intensified oxidative stress, leading to pyroptosis and mtDNA release. Unlike traditional catalytic therapies constrained by H_2O_2 limitations, $GOCoF_2$ utilized GOx-mediated glucose consumption to generate H_2O_2 and ROS in a self-perpetuating cycle. This metabolic modulation strategy not only initiated pyroptosis but also alleviated TREX2-mediated inhibition of the cGAS-STING pathway, which was a typically glucose-dependent. The Co^{2+} component further augments STING pathway activation, effectively linking metabolic alterations with immune stimulation and transforming immunologically inert tumors into immunologically active tumors. When combined with α-PD-1 immunotherapy, $GOCoF_2$ demonstrated significant systemic immune activation, addressing the constraints of immune checkpoint blockade monotherapy.

The localized administration of the $GOCoF_2$ nanoadjuvant, a powerful immune-stimulatory agent, may be identified as the optimal approach for generating potent antitumor immunity while reducing the likelihood of systemic immune hyperactivation and subsequent cytokine release syndrome. Additionally, our research revealed that $GOCoF_2$ can potentiate TAE therapy, a primary treatment modality for inoperable HCC. By capitalizing on tumor metabolic characteristics, $GOCoF_2$ converts glucose into a therapeutic advantage through sequential catalytic processes, thereby strengthening the pyroptosis-STING axis and enhancing tumor suppression. This investigation not only highlighted the therapeutic value of metabolic reprogramming in cancer immunotherapy but also established a framework for developing nanocatalytic systems that target tumor-specific metabolic weaknesses. The effective implementation of $GOCoF_2$ in TAE protocols further confirmed its clinical applicability, opening new avenues for advanced interventional immunotherapies against progressive malignancies. These discoveries reveal a complex interaction among metabolic regulation, pyroptosis induction, and STING pathway stimulation, offering a strategic model for next-generation nanotherapeutic approach focused on the metabolic-immunological axis in solid tumors.

CRediT authorship contribution statement

Linzhu Zhang: Writing – original draft, Formal analysis, Data curation. **Di Wang:** Formal analysis, Data curation. **Yiming Liu:** Formal analysis, Data curation. **Nailin Yang:** Writing – review & editing, Project administration. **Shumin Sun:** Formal analysis, Data curation. **Chunjie Wang:** Formal analysis, Data curation. **Duo Wang:** Formal analysis, Data curation. **Jihu Nie:** Formal analysis, Data curation. **Juan Qin:** Formal analysis, Data curation. **Lei Zhang:** Writing – review & editing, Resources, Project administration. **Liang Cheng:** Writing –

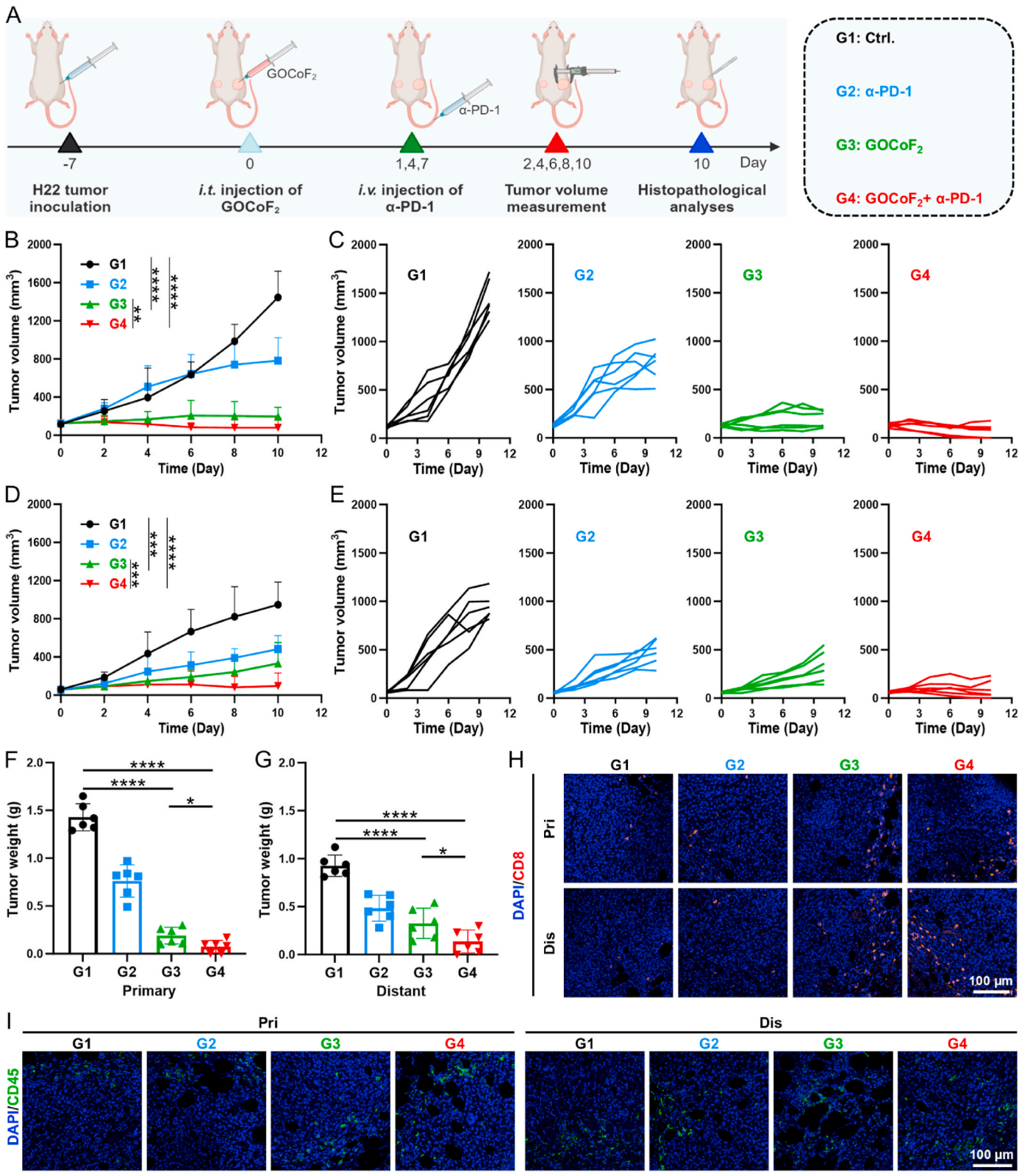

Fig. 6. $GOCoF_2$ induced metabolic-pyroptotic-immunotherapy combined with α-PD-1 treatment. A) Schematic illustration of the in vivo treatment procedure in mice. G1: Ctrl., G2: α-PD-1, G3: $GOCoF_2$, G4: $GOCoF_2$ + α-PD-1. **B)** Changes in the volume of primary H22 tumors after different treatments. **C)** Individual growth curves of H22 primary tumors after various treatments. **D)** Changes in the volume of distant H22 tumors after different treatments. **E)** Individual growth curves of H22 distant tumors after various treatments. **F)** Weight changes in the primary tumor and **G)** distant tumor after different treatments. **H)** Images of the primary tumor and distant tumor slices after fluorescence staining for $CD8^+$ and **I)** $CD45^+$ cells obtained from mice subjected to different treatments. The data are presented as the mean values ± SD. The P values indicated in the figure were determined by employing the two-tailed student's t-test. *p < 0.05, **p < 0.01, ***p < 0.001, ****p < 0.0001.

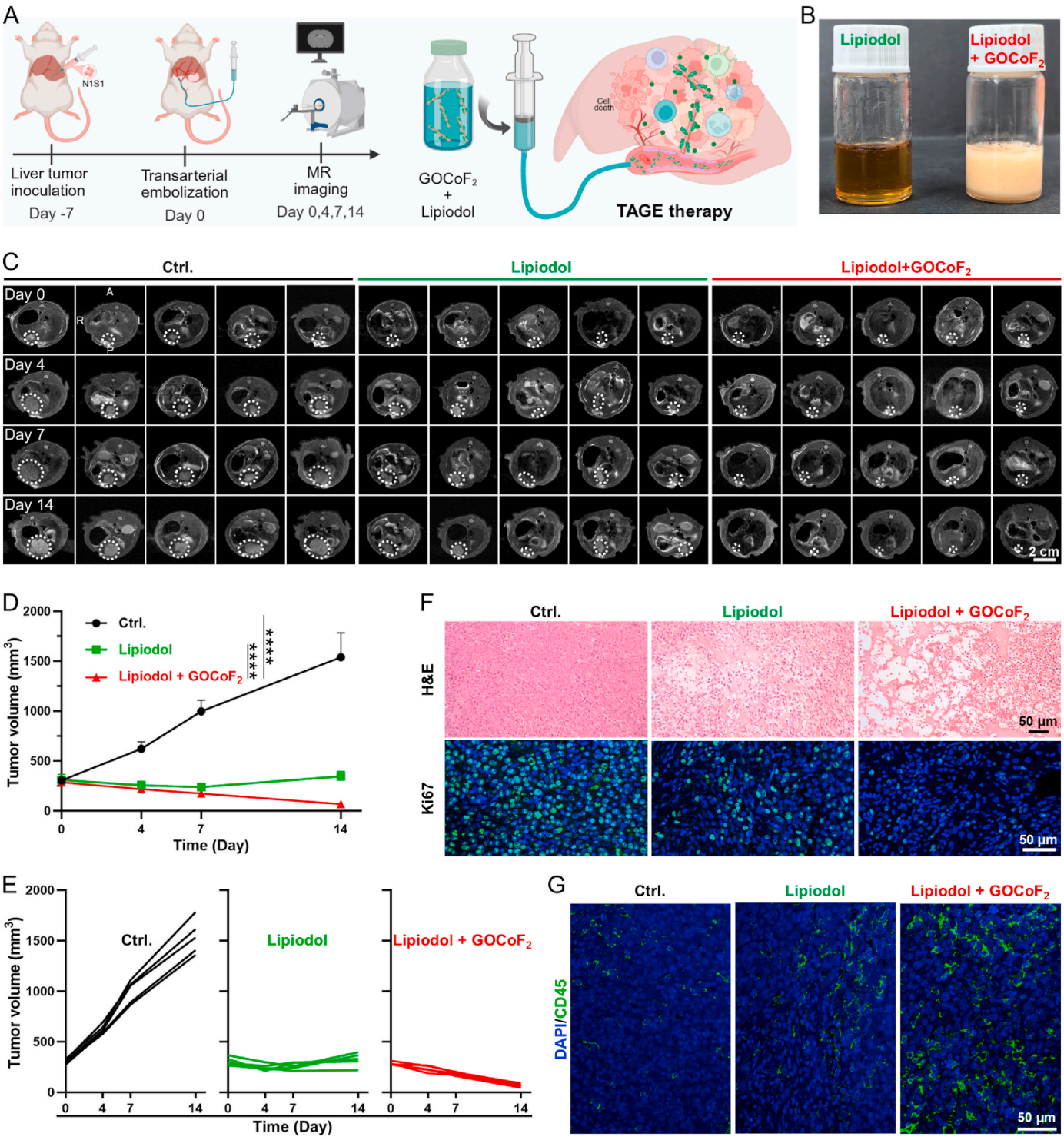

Fig. 7. Embolization therapy of rat orthotopic HCC with $GOCoF_2$ mixed with lipiodol. A) A schematic diagram of the TAGE treatment schedule in N1S1-bearing rats. **B)** Photograph of $GOCoF_2$ + Lipiodol. **C)** Representative T2 contrast-enhanced MR images of N1S1-bearing rats after various treatments. L: Left, R: Right, A: Anterior, P: Posterior. **D)** Changes in the tumor growth curve after different treatments. **E)** Individual growth curves of N1S1 tumors after various treatments. **F)** Representative images of H&E and Ki-67 staining of mouse tumor sections after various treatments. **G)** Fluorescence staining of $CD45^+$cells in the N1S1 liver mice with various groups. The data are presented as the mean values ± SD. The P values indicated in the figure were determined by employing the two-tailed student's t-test. ****$p < 0.0001$.

review & editing, Supervision, Project administration. **Haidong Zhu:** Supervision, Funding acquisition.

Ethics approval and consent to participate

All animal experiments were approved by the Animal Care and Use Committee of Soochow University (approval number: 202409A0028), and all protocols adhered strictly to the Guide for the Care and Use of

Laboratory Animals.

Declaration of competing interest

The authors declare that they have no known competing financial interests or personal relationships that could have appeared to influence the work reported in this paper.

Acknowledgements

This article was partially supported by the National Key R&D Program of China (No. 2023YFC2413500), National Natural Science Foundation of China (52472288, 52403386, 82072039, 82372067), Collaborative Innovation Center of Radiological Medicine of Jiangsu Higher Education Institutions (FY202302), Collaborative Innovation Center of Suzhou Nano Science and Technology, Suzhou Key Laboratory of Nanotechnology and Biomedicine, 111 Project, and Joint International Research Laboratory of Carbon-Based Functional Materials and Devices, Medical Research Project of Jiangsu Province (ZD2022024). N. Y. was supported by the Macao Young Scholars Program and the Jiangsu Funding Program for Excellent Postdoctoral Talent. L.Z. was supported by the SEU Innovation Capability Enhancement Plan for Doctoral Students (CXJH_SEU 25229) and Postgraduate Research&Practice Innovation Program of Jiangsu Province (KYCX25_0523).

Appendix A. Supplementary data

Supplementary data to this article can be found online at https://doi.org/10.1016/j.bioactmat.2025.07.040.

References

[1] R.L. Siegel, A.N. Giaquinto, A. Jemal, Cancer statistics, CA Cancer J. Clin. 74 (1) (2024) 12–49, 2024.
[2] J.M. Llovet, F. Castet, M. Heikenwalder, M.K. Maini, V. Mazzaferro, D.J. Pinato, E. Pikarsky, A.X. Zhu, R.S. Finn, Immunotherapies for hepatocellular carcinoma, Nat. Rev. Clin. Oncol. 19 (3) (2022) 151–172.
[3] H.-D. Zhu, H.-L. Li, M.-S. Huang, W.-Z. Yang, G.-W. Yin, B.-Y. Zhong, J.-H. Sun, Z.-C. Jin, J.-J. Chen, N.-J. Ge, Transarterial chemoembolization with PD-(L) 1 inhibitors plus molecular targeted therapies for hepatocellular carcinoma (CHANCE001), Signal Transduct. Targeted Ther. 8 (1) (2023) 58.
[4] Z.-C. Jin, J.-J. Chen, X.-L. Zhu, X.-H. Duan, Y.-J. Xin, B.-Y. Zhong, J.-Z. Chen, J. Tie, K.-S. Zhu, L. Zhang, Immune checkpoint inhibitors and anti-vascular endothelial growth factor antibody/tyrosine kinase inhibitors with or without transarterial chemoembolization as first-line treatment for advanced hepatocellular carcinoma (CHANCE2201): a target trial emulation study, eClinicalMedicine 72 (2024) 102622.
[5] N. Yang, X. Sun, Y. Zhou, X. Yang, J. You, Z. Yu, J. Ge, F. Gong, Z. Xiao, Y. Jin, Liquid metal microspheres with an eddy-thermal effect for magnetic hyperthermia-enhanced cancer embolization-immunotherapy, Sci. Bull. 68 (16) (2023) 1772–1783.
[6] Z. Peng, W. Fan, B. Zhu, G. Wang, J. Sun, C. Xiao, F. Huang, R. Tang, Y. Cheng, Z. Huang, Lenvatinib combined with transarterial chemoembolization as first-line treatment for advanced hepatocellular carcinoma: a phase III, randomized clinical trial (LAUNCH), J. Clin. Oncol. 41 (1) (2023) 117–127.
[7] E.N. Arner, J.C. Rathmell, Metabolic programming and immune suppression in the tumor microenvironment, Cancer Cell 41 (3) (2023) 421–433.
[8] M. Li, X. Luo, S. Lei, Y. Liu, H. Guo, Y. Zhang, Y. Pan, K. Chen, J. Lin, P. Huang, Synchronous interventions of glucose and mitochondrial metabolisms for antitumor bioenergetic therapy, Adv. Mater. 35 (29) (2023) 2301099.
[9] Y. Wang, G.J. Patti, The Warburg effect: a signature of mitochondrial overload, Trends Cell Biol. 33 (12) (2023) 1014–1020.
[10] L.H. Fu, Y. Wan, C. Qi, J. He, C. Li, C. Yang, H. Xu, J. Lin, P. Huang, Nanocatalytic theranostics with glutathione depletion and enhanced reactive oxygen species generation for efficient cancer therapy, Adv. Mater. 33 (7) (2021) 2006892.
[11] Y. Zhang, S. Jiang, J. Lin, P. Huang, Antineoplastic enzyme as drug carrier with activatable catalytic activity for efficient combined therapy, Angew. Chem., Int. Ed. 61 (41) (2022) e202208583.
[12] Y. Niu, F.J. Stadler, T. He, X. Zhang, Y. Yu, S. Chen, Smart multifunctional polyurethane microcapsules for the quick release of anticancer drugs in BGC 823 and HeLa tumor cells, J. Mater. Chem. B 5 (48) (2017) 9477–9481.
[13] L.H. Fu, C. Qi, T. Sun, K. Huang, J. Lin, P. Huang, Glucose oxidase-instructed biomineralization of calcium-based biomaterials for biomedical applications, Explorations 3 (6) (2023) 20210110.
[14] S. Sun, N. Yang, Z. Pei, F. Gong, L. Cheng, Biomedical engineering targeting cancer stem cells to reinforce cancer therapy, Coord. Chem. Rev. 530 (2025) 216494.
[15] N. Yang, S. Sun, J. Xu, F. Gong, H. Lei, Y. Hao, Z. Pei, C. Wang, Q. Yu, J. Nie, Manganese galvanic cells intervene in tumor metabolism to reinforce cGAS-STING activation for bidirectional synergistic hydrogen-immunotherapy, Adv. Mater. 37 (8) (2025) 2414929.
[16] J. Zheng, J. Zhang, T. Zhang, Y. Yan, S. Bi, Automatic metabolism modulator for glycolytic intervention-induced Cascade cancer therapy, BMEMat 3 (1) (2025) e70006.
[17] M. De Martino, J.C. Rathmell, L. Galluzzi, C. Vanpouille-Box, Cancer cell metabolism and antitumour immunity, Nat. Rev. Immunol. 24 (9) (2024) 654–669.
[18] H. Zhao, Y. Zhang, Y. Sun, Z. Zhu, J. Ren, X. Qu, Self-Driven CuAAC reaction catalyzed by photosensitive biohybrids energized by lactate for boosting CancerImmunotherapy, Angew. Chem., Int. Ed. 64 (20) (2025) e202425018.
[19] J. Ma, L. Tang, Y. Tan, J. Xiao, K. Wei, X. Zhang, Y. Ma, S. Tong, J. Chen, N. Zhou, Lithium carbonate revitalizes tumor-reactive CD8+ T cells by shunting lactic acid into mitochondria, Nat. Immunol. 25 (3) (2024) 552–561.
[20] N.T. Nguyen, S. Gevers, R.N. Kok, L.M. Burgering, H. Neikes, N. Akkerman, M. A. Betjes, M.C. Ludikhuize, C. Gulersonmez, E.C. Stigter, Lactate controls cancer stemness and plasticity through epigenetic regulation, Cell Metab. 37 (4) (2025) 903–919.
[21] K. Newton, A. Strasser, N. Kayagaki, V.M. Dixit, Cell death, Cell 187 (2) (2024) 235–256.
[22] Y. Liu, R. Pan, Y. Ouyang, W. Gu, T. Xiao, H. Yang, L. Tang, H. Wang, B. Xiang, P. Chen, Pyroptosis in health and disease: mechanisms, regulation and clinical perspective, Signal Transduct. Targeted Ther. 9 (1) (2024) 245.
[23] W.-D. Wang, Z.-J. Sun, Evoking pyroptosis with nanomaterials for cancer immunotherapy: current boom and novel outlook, Nano Trans.Med. 1 (1) (2022) e9130001.
[24] S. Zeng, J. Wang, H. Kang, H. Li, X. Peng, J. Yoon, Photon-Driven dye induction pyroptosis: an emerging anti-tumor immunotherapy paradigm, Angew. Chem., Int. Ed. 137 (2) (2025) e202417899.
[25] P. Zheng, G. Wang, B. Liu, H. Ding, B. Ding, J. Lin, Succinate nanomaterials boost tumor immunotherapy via activating cell pyroptosis and enhancing MHC-I expression, J. Am. Chem. Soc. 147 (2) (2025) 1508–1517.
[26] K. Xu, M. Chang, Z. Wang, H. Yang, Y. Jia, W. Xu, B. Zhao, Y. Chen, F. Yao, Multienzyme-Mimicking LaCoO3 nanotrigger for programming cancer-cell pyroptosis, Adv. Mater. 35 (35) (2023) 2302961.
[27] D. Wang, L. Zhang, J. Nie, N. Yang, S. Sun, C. Wang, Z. Pei, F. Gong, X. Sun, Y. Jin, L. Cheng, Engineered nano-micro pyroptosis generators: a magnetic-metallo-immunotherapeutic strategy to reinforce transarterial embolization, J. Am. Chem. Soc. 147 (2025) 25536–25552.
[28] F. Wang, Y. Fan, Y. Liu, X. Lou, L. Sutrisno, S. Peng, J. Li, Oxygen-carrying semiconducting polymer nanoprodrugs induce sono-pyroptosis for deep-tissue tumor treatment, Explorations 4 (4) (2024) 20230100.
[29] J. Kim, Y. Xu, J.H. Lim, J.Y. Lee, M. Li, J.M. Fox, M. Vendrell, J.S. Kim, Bioorthogonal activation of deep red photoredox catalysis inducing pyroptosis, J. Am. Chem. Soc. 147 (1) (2024) 701–712.
[30] M. Li, J. Kim, H. Rha, S. Son, M.S. Levine, Y. Xu, J.L. Sessler, J.S. Kim, Photon-controlled pyroptosis activation (photopyro): an emerging trigger for antitumor immune response, J. Am. Chem. Soc. 145 (11) (2023) 6007–6023.
[31] B. Ding, H. Chen, J. Tan, Q. Meng, P. Zheng, P.a. Ma, J. Lin, ZIF-8 nanoparticles evoke pyroptosis for high-efficiency cancer immunotherapy, Angew. Chem., Int. Ed. 62 (10) (2023) e202215307.
[32] Q. Yu, S. Sun, N. Yang, Z. Pei, Y. Chen, J. Nie, H. Lei, L. Wang, F. Gong, L. Cheng, Self-Cascaded Pyroptosis-STING initiators for catalytic metalloimmunotherapy, J. Am. Chem. Soc. 147 (4) (2025) 3161–3173.
[33] J. Nie, N. Yang, S. Sun, L. Wang, Z. Pei, J. Wu, Q. Yu, Z. Han, Y. Chen, L. Cheng, Antimony component schottky nanoheterojunctions as ultrasound-heightened pyroptosis initiators for sonocatalytic immunotherapy, Angew. Chem., Int. Ed. 64 (4) (2025) e202416426.
[34] S. Sun, X. Huang, N. Yang, H. Lei, Z. Pei, Z. Han, L. Liu, F. Gong, Q. Yu, J. Li, Fluorinated Titanium oxide (TiO2–xFx) nanospindles as ultrasound-triggered pyroptosis inducers to boost sonodynamic immunotherapy, ACS Nano 18 (30) (2024) 19756–19770.
[35] X. Han, S. Sun, N. Yang, Z. Han, Z. Pei, Q. Yu, J. Nie, L. Wang, A. Liu, X. Meng, Nano-Engineered magnesium implants for magnetothermal enhanced pyroptosis to boost immunotherapy, Adv. Funct. Mater. 34 (46) (2024) 2405836.
[36] B. Wang, G. Zhang, Z. Chen, H. Shen, C. Li, J. Li, M. Yi, J. Sun, R.T. Kwok, J. W. Lam, Lab-in-Cell: a covalent photosensitizer reverses hypoxia and evokes ferroptosis and pyroptosis for enhanced anti-tumor immunity, Adv. Mater. 37 (13) (2025) 2415673.
[37] Z. Chen, L. Zhao, W. Guo, L. Tan, Q. Wu, C. Fu, X. Ren, S. Yu, X. Chen, N.-Y. Kim, Microwave-sensitive Al-based nano-immunoadjuvant for strengthened tumor microwave-immunotherapy via programmed activation of NLRP3-mediated pyroptosis, Chin. Chem. Lett. (2025) 111299.
[38] J. Wu, Y. Meng, F. Wu, J. Shi, Q. Sun, X. Jiang, Y. Liu, P. Zhao, Q. Wang, L. Guo, Ultrasound-Driven Non-Metallic Fenton-active center construction for extensive chemodynamic therapy, Adv. Mater. 36 (2) (2024) 2307980.
[39] X. Zhang, X. Chen, Y. Zhao, Nanozymes: versatile platforms for cancer diagnosis and therapy, Nano-Micro Lett. 14 (1) (2022) 95.
[40] S. Zhang, N. Yang, S. Sun, H. Zhao, W. Wang, J. Nie, Z. Pei, W. He, L. Zhang, L. Cheng, Dually fluorinated unimolecular micelles for stable oxygen-carrying and enhanced photosensitive efficiency to boost photodynamic therapy against hypoxic tumors, Acta Biomater. 193 (2025) 406–416.
[41] G. Xiong, D. Huang, L. Lu, X. Luo, Y. Wang, S. Liu, M. Chen, S. Yu, M. Kappen, C. You, Near-infrared-II light induced mild hyperthermia activate cisplatin-

artemisinin nanoparticle for enhanced chemo/chemodynamic therapy and immunotherapy, Small Methods 6 (9) (2022) 2200379.
[42] Y. Wei, Q. Miao, M. Zhang, W. Zhang, M. Shi, R. Liu, J. Su, P. Sun, Y. Zhao, PtCu nanozyme integrating single atom Pt and Pt subnanoclusters for the sustained treatment of cutaneous melanoma, Chin. Chem. Lett. (2025) 111164.
[43] N. Yang, F. Gong, Y. Zhou, Y. Hao, Z. Dong, H. Lei, L. Zhong, X. Yang, X. Wang, Y. Zhao, A general in-situ reduction method to prepare core-shell liquid-metal/metal nanoparticles for photothermally enhanced catalytic cancer therapy, Biomaterials 277 (2021) 121125.
[44] S. Zhang, X.J. Gao, Y. Ma, K. Song, M. Ge, S. Ma, L. Zhang, Y. Yuan, W. Jiang, Z. Wu, A bioinspired sulfur–Fe–heme nanozyme with selective peroxidase-like activity for enhanced tumor chemotherapy, Nat. Commun. 15 (1) (2024) 1–21.
[45] Y. Liu, R. Niu, H. Zhao, Y. Wang, S. Song, H. Zhang, Y. Zhao, Single-site nanozymes with a highly conjugated coordination structure for antitumor immunotherapy via cuproptosis and cascade-enhanced T lymphocyte activity, J. Am. Chem. Soc. 146 (6) (2024) 3675–3688.
[46] H. Wang, W. Ouyang, H. Liu, Tumor microenvironment responsive nanozymes for multimodal imaging of tumors, Nano Trans.Med. 3 (2024) 100032.
[47] J. Tang, Y. Liu, Y. Xue, Z. Jiang, B. Chen, J. Liu, Endoperoxide-enhanced self-assembled ROS producer as intracellular prodrugs for tumor chemotherapy and chemodynamic therapy, Explorations 4 (4) (2024) 20230127.
[48] S. Cai, J. Liu, J. Ding, Z. Fu, H. Li, Y. Xiong, Z. Lian, R. Yang, C. Chen, Tumor-microenvironment-responsive Cascade reactions by a cobalt-single-atom nanozyme for synergistic nanocatalytic chemotherapy, Angew. Chem., Int. Ed. 134 (48) (2022) e202204502.
[49] Z. Chu, J. Yang, W. Zheng, J. Sun, W. Wang, H. Qian, Recent advances on modulation of H2O2 in tumor microenvironment for enhanced cancer therapeutic efficacy, Coord. Chem. Rev. 481 (2023) 215049.
[50] R. Miao, C. Jiang, W.Y. Chang, H. Zhang, J. An, F. Ho, P. Chen, H. Zhang, C. Junqueira, D. Amgalan, Gasdermin D permeabilization of mitochondrial inner and outer membranes accelerates and enhances pyroptosis, Immunity 56 (11) (2023) 2523–2541. e8.
[51] Z. Li, X. Li, Y. Lu, X. Zhu, W. Zheng, K. Chen, X. Wang, T. Wang, W. Guan, Z. Su, Novel Photo-STING agonists delivered by erythrocyte efferocytosis-mimicking pattern to repolarize tumor-associated macrophages for boosting anticancer immunotherapy, Adv. Mater. 36 (47) (2024) 2410937.
[52] X. Zhao, R. Zheng, B. Zhang, Y. Zhao, W. Xue, Y. Fang, Y. Huang, M. Yin, Sulfonated perylene as Three-in-One STING agonist for cancer chemo-immunotherapy, Angew. Chem., Int. Ed. 63 (11) (2024) e202318799.
[53] Z. Pei, N. Jiang, F. Gong, W. Yang, J. Xu, B. Yu, N. Yang, J. Wu, H. Lei, S. Sun, A metal anion strategy to induce pyroptosis combined with STING activation to synergistically amplify anti-tumor immunity, Mater. Today 80 (2024) 23–39.
[54] X. Li, H. Liu, W. Gao, Q. Yang, X. Li, X. Zhou, L. Wang, Z. Lu, J. Liu, A. Luo, Octadecyl gallate and lipid-modified MnSe2 nanoparticles enhance radiosensitivity in esophageal squamous cell carcinoma and promote radioprotection in normal tissues, Adv. Mater. 36 (23) (2024) 2311291.
[55] Y. Huang, G. Qin, T. Cui, C. Zhao, J. Ren, X. Qu, A bimetallic nanoplatform for STING activation and CRISPR/Cas mediated depletion of the methionine transporter in cancer cells restores anti-tumor immune responses, Nat. Commun. 14 (1) (2023) 4647.
[56] J. Wang, S. Li, M. Wang, X. Wang, S. Chen, Z. Sun, X. Ren, G. Huang, B.D. Sumer, N. Yan, STING licensing of type I dendritic cells potentiates antitumor immunity, Sci. Immunol. 9 (92) (2024) eadj3945.
[57] M. Shen, Y. Wang, T. Bing, Y. Tang, X. Liu, Y. Yu, Alendronate triggered dual-cascade targeting prodrug nanoparticles for enhanced tumor penetration and STING activation of osteosarcoma, Adv. Funct. Mater. 33 (49) (2023) 2307013.
[58] T. Guan, Z. Chen, X. Wang, S. Gao, X. Lu, Y. Li, Z. Wang, S. Zhang, Y. Guo, M. Guo, Harnessing Mn2+ ions and antitumor peptides: a robust hydrogel for enhanced tumor immunotherapy, J. Am. Chem. Soc. 147 (8) (2025) 6523–6535.
[59] X. Sun, X. Zhou, X. Shi, O.A. Abed, X. An, Y.L. Lei, J.J. Moon, Strategies for the development of metalloimmunotherapies, Nat. Biomed. Eng. 8 (9) (2024) 1073–1091.
[60] C. Wang, L. Zhong, J. Xu, Q. Zhuang, F. Gong, X. Chen, H. Tao, C. Hu, F. Huang, N. Yang, Oncolytic mineralized bacteria as potent locally administered immunotherapeutics, Nat. Biomed. Eng. 8 (5) (2024) 561–578.
[61] Y. Luo, X. He, Q. Du, L. Xu, J. Xu, J. Wang, W. Zhang, Y. Zhong, D. Guo, Y. Liu, Metal-based smart nanosystems in cancer immunotherapy, Explorations 4 (6) (2024) 20230134.
[62] W. Zhang, X. Hu, W. Cheng, L. Zhang, Y. Chen, Q. Fu, L. Liu, S. Fan, Harnessing nanomaterials to precisely regulate the immunosuppressive tumor microenvironment for enhanced immunotherapy, BMEMat (2025) e70019.
[63] G. Zhang, N. Wang, Y. Ma, S. Zhai, T. Ngai, S. Ni, X. Jiang, J. Jiao, J. Cui, Metal coordination-driven assembly of stimulator of interferon genes-activating nanoparticles for tumor chemo-immunotherapy, BMEMat 2 (2) (2024) e12106.
[64] T. Chen, Z.-G. Xu, J. Luo, R.K. Manne, Z. Wang, C.-C. Hsu, B.-S. Pan, Z. Cai, P.-J. Tsai, Y.-S. Tsai, NSUN2 is a glucose sensor suppressing cGAS/STING to maintain tumorigenesis and immunotherapy resistance, Cell Metab. 35 (10) (2023) 1782–1798. e8.
[65] L. Zhang, C. Jiang, Y. Zhong, K. Sun, H. Jing, J. Song, J. Xie, Y. Zhou, M. Tian, C. Zhang, STING is a cell-intrinsic metabolic checkpoint restricting aerobic glycolysis by targeting HK2, Nat. Cell Biol. 25 (8) (2023) 1208–1222.
[66] J. Yang, T. Su, Q. Wang, R. Shi, J. Ding, X. Chen, Glucose metabolism-targeted poly (amino acid) nanoformulation of Oxaliplatin (IV)-Aspirin prodrug for enhanced chemo-immunotherapy, Adv. Mater. 37 (12) (2025) 2419033.
[67] A.J. Korman, S.C. Garrett-Thomson, N. Lonberg, The foundations of immune checkpoint blockade and the ipilimumab approval decennial, Nat. Rev. Drug Discov. 21 (7) (2022) 509–528.
[68] N. Yang, F. Gong, B. Liu, Y. Hao, Y. Chao, H. Lei, X. Yang, Y. Gong, X. Wang, Z. Liu, Magnesium galvanic cells produce hydrogen and modulate the tumor microenvironment to inhibit cancer growth, Nat. Commun. 13 (1) (2022) 2336.
[69] J. Ge, N. Yang, Y. Yang, H. Yu, X. Yang, Y. Wang, T. Wang, S. Cheng, Y. Wang, Z. Han, The combination of eddy thermal effect of biodegradable magnesium with immune checkpoint blockade shows enhanced efficacy against osteosarcoma, Bioact. Mater. 25 (2023) 73–85.
[70] L. Lei, P. Liu, W. Jing, Z. Wu, Advancements in modifying the efficacy of immunotherapies through the thermal effects of nanomaterials, Nano Trans.Med. 2 (4) (2023) 100022.
[71] D. Wang, L. Zhang, W.H. Yang, L.Z. Zhang, C. Yu, J. Qin, L.Z. Feng, Z. Liu, G. J. Teng, Arginine-Loaded nano-calcium-phosphate-stabilized lipiodol pickering emulsions potentiates transarterial embolization-immunotherapy, Adv. Sci. 12 (6) (2025) 2410484.